AIE Polymer Micelle/Vesicle Photocatalysts Combined with Native Enzymes for Aerobic Photobiocatalysis

Nian Zhang, Sylvain Trépout, Hui Chen, Min-Hui Li

▶ **To cite this version:**

Nian Zhang, Sylvain Trépout, Hui Chen, Min-Hui Li. AIE Polymer Micelle/Vesicle Photocatalysts Combined with Native Enzymes for Aerobic Photobiocatalysis. Journal of the American Chemical Society, 2023, 145 (1), pp.288-299. 10.1021/jacs.2c09933 . hal-04246873

HAL Id: hal-04246873
https://hal.science/hal-04246873v1

Submitted on 18 Oct 2023

HAL is a multi-disciplinary open access archive for the deposit and dissemination of scientific research documents, whether they are published or not. The documents may come from teaching and research institutions in France or abroad, or from public or private research centers.

L'archive ouverte pluridisciplinaire **HAL**, est destinée au dépôt et à la diffusion de documents scientifiques de niveau recherche, publiés ou non, émanant des établissements d'enseignement et de recherche français ou étrangers, des laboratoires publics ou privés.

AIE Polymer Micelles/Vesicles Photocatalysts Combined with Native Enzymes for Aerobic Photobiocatalysis

Nian Zhang,[a] Sylvain Trépout,[b] Hui Chen,*[a] and Min-Hui Li*[a]

[a] Chimie ParisTech, PSL Université Paris, CNRS, Institut de Recherche de Chimie Paris, UMR8247, 11 rue Pierre et Marie Curie, 75005, Paris, France.

[b] Institut Curie, Université Paris-Saclay, Inserm US43, CNRS UMS2016, Centre Universitaire, Bât. 101B-110-111-112, Rue Henri Becquerel, CS 90030, 91401 Orsay Cedex, France.

ABSTRACT: Biocatalytic transformation has attracted increasing attention in the green synthesis of chemicals due to the diversity of enzymes, their high catalytic activities and specificities, and environmentally benign conditions. Most redox enzymes in nature are dependent on nicotinamide cofactors like NAD^+/NADH. The use of solar energy, especially the visible light, in the regeneration of cofactors through the combination of photocatalysis and biocatalysis provides an extraordinary opportunity to make complete green processes. However, the combination of photocatalysts and enzymes has been challenged by the rapid degradation and deactivation of the enzymatic material by photogenerated reactive oxygen species (ROS). Here, we design core-shell structured polymer micelles and vesicles with aggregation-induced emission (AIE) as visible-light-mediated photocatalysts for highly stable and recyclable photobiocatalysis under aerobic conditions. The NAD^+ from NADH can be efficiently regenerated by the photoactive hydrophobic core of polymer micelles and the hydrophobic membrane of the polymer vesicles, while the enzymatic material (glucose 1-dehydrogenase) is screened from the attack of photogenerated ROS by the hydrophilic surface layer of polymer colloids. After at least 10 regeneration cycles, the enzyme keeps its active state, meanwhile polymer micelles and vesicles maintain their photocatalytic activity. These polymer colloids show the potential to be developed for the implementation of industrially relevant photobiocatalytic systems.

INTRODUCTION

Photobiocatalytic systems can be widely considered as those photocatalytic systems consisting of an enzyme, which enables the biocatalytic transformation under the tandem action of enzyme.[1] Green algae and plants are natural photobiocatalytic systems par excellence, which has developed a very complex machinery through evolution to convert sunlight into high-energy biochemical compounds.[2] Biocatalytic transformation has attracted increasing attention in the green synthesis of chemicals due to the diversity of enzymes, their high catalytic activities and specificities, and environmentally benign conditions (*e.g.*, aqueous media, ambient temperature and pressure, neutral pH). The use of solar energy in chemical synthesis through the combination of photocatalysis and biocatalysis provides an extraordinary opportunity to make complete green processes.

Redox enzymes (or oxidoreductases) that play a key role in biological energy transduction can be used to catalyze various synthetically useful redox reactions, [1-3] such as asymmetric reduction of carbonyl groups, oxygenation of C-H bonds, epoxidation of C=C bonds, and Baeyer–Villiger oxidation.[4-6] These redox reactions can be applied in the synthesis of pharmaceuticals, food additives, and fuels.[7] For example, the oxidation of alcohol is a crucial reaction in organic synthesis, and alcohol dehydrogenase can carry out highly selective conversions of primary alcohols to either aldehydes or acids.[8-10] However, over 80% of oxidoreductases in nature are dependent on nicotinamide cofactors NADH/NAD^+ (β-nicotinamide adenine dinucleotide) or NADPH/$NADP^+$ (β-nicotinamide adenine dinucleotide phosphate) for their catalytic activities. Nature has developed complicated electron transport chains to regenerate the required cofactor species,[11] while the mimic of these natural processes is extremely challenging for synthetic systems. Therefore, alternative cofactor regeneration pathways have been investigated, for example, through enzymatic, chemical, electrochemical, or photochemical methods.[5, 12-14] Among them, photochemical method using visible light is an attractive and green way.

Visible-light-mediated photocatalysis has been largely developed to catalyze reactions under mild conditions, using mainly photocatalysts based on either transition metals [15] or organic catalysts [16]. Recently, photocatalytic systems in different forms like free organic dye molecules, polymers, nano or micro-particles, covalent organic frameworks (COFs) or metal organic frameworks (MOFs) have been implemented for cofactor regeneration.[17] Unfortunately, these photocatalytic systems in normal aerobic enzymatic systems also produce reactive oxygen species (ROS), which actually limit the combination of these materials with enzymes because of the rapid degradation of the biomaterial caused by ROS. Compartmentalization strategies have been developed to prevent the deactivation and degradation of enzymes.[18-20] For example, the immobilization of the enzymes or photocatalysts within silica nanoparticles has been used to avoid the contact of ROS with the biomaterial.[18-19] Superoxide dismutase and catalase were also co-encapsulated together with the enzyme to further protect the active enzymatic material.[20] However, the enzyme immo-

bilization within solid nanoparticles can significantly decrease its efficiency compared to the native enzyme. Recently, core−shell porous nano-photoreactors were designed, where cofactor NAD^+ was efficiently regenerated from NADH by the photoactive organosilica core, while the enzyme was screened from the photogenerated ROS by the non-photoactive organosilica shell.[21] Nevertheless, this inorganic core-shell strategy requires complicated elaboration of core and shell structures.

Polymer micelles and vesicles are also core-shell structures with hydrophilic polymer shell and hydrophobic polymer core formed by simple self-assembly of amphiphilic block copolymers (in vesicles, the core and the shell correspond, respectively, to the hydrophobic inner part and the hydrophilic outer layers of the membrane). It is worth mentioning that recently photocatalysis on lipid membranes of liposomes has been reported to mimic and understand natural photosynthesis and the role of the membrane in it.[22-24] Here, in polymer micelles and vesicles, the hydrophobic block can be designed as a photocatalytic polymer, and the hydrophobic cores constitute then nano-photoreactors. The mass transportation of hydrophilic $NADH/NAD^+$ within the hydrophilic polymer layer could be free. In contrast, large size enzymes could not diffuse into hydrophilic layer. Considering the relatively short lifetime of ROS, hydrophilic polymer shell with the appropriate thickness could be designed to trap and deactivate those photogenerated ROS to protect the active enzyme soluble in water. Therefore, these polymer micelles and vesicles readily dispersed in aqueous media could be promising and efficient photocatalytic materials for aerobic photobiocatalysis. For the photocatalytic polymer, a metal-free organic dye was intended as a side group to attach to the polymer backbone. As the visible-light-mediated photocatalysis is a prerequisite in this work, rose Bengal and similar dyes like eosin Y and erythrosine could be interesting candidates.[16] Nevertheless, the use of these classical hydrophobic dyes in hydrophilic media presents a problem known as aggregation-caused quenching (ACQ),[25] because of their extended π conjugation and intrinsically planar structure. This structural feature leads to suppressed luminescence emission and to nonradiative decay in the aggregated state. The nonradiative decay pathways could

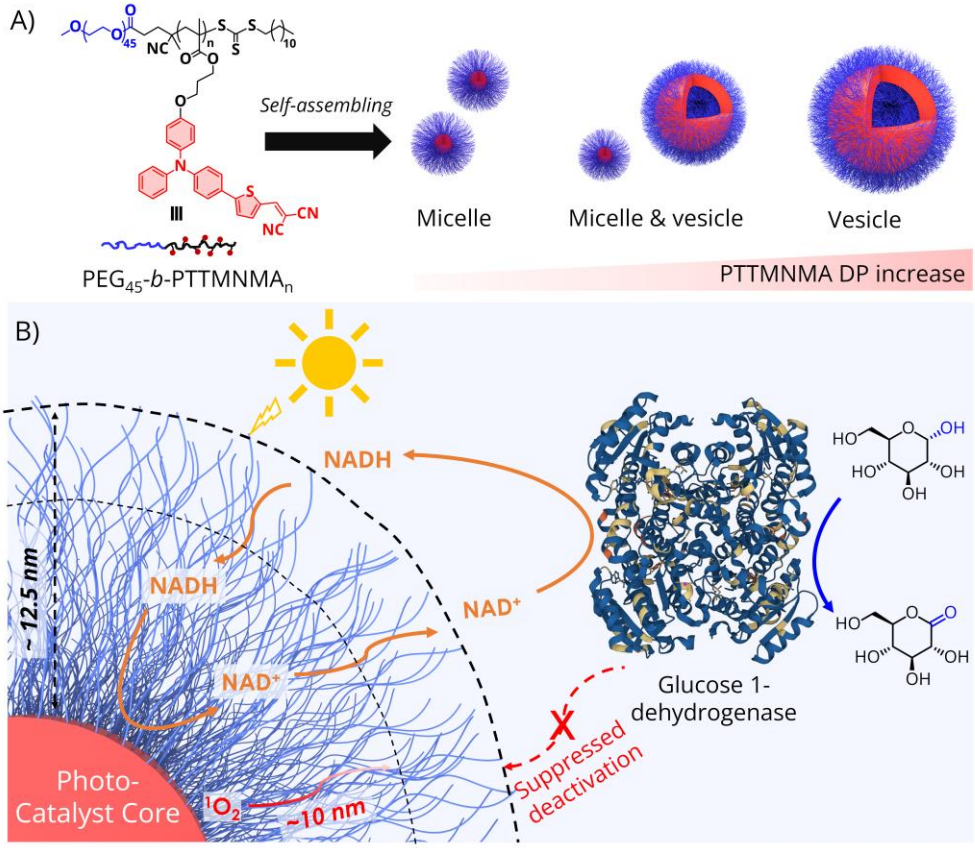

Figure 1. (A) The chemical structure of TTMN-based AIE block copolymers and their micelles and vesicles models. (B) Schematic representation of the aerobic photobiocatalysis system with the combination of micelle/vesicle photocatalyst and glucose 1-dehydrogenase to perform the photobiocatalytic tandem reactions in an aqueous solution. The enzyme maintains its activity because the hydrophilic PEG layer servers as a shield (thickness H ~ 8.6 nm to 12.5 nm) to avoid the contact between enzyme and photogenerated ROS ($^1O_2$ etc.) (diffusion distance ~ 10 nm).

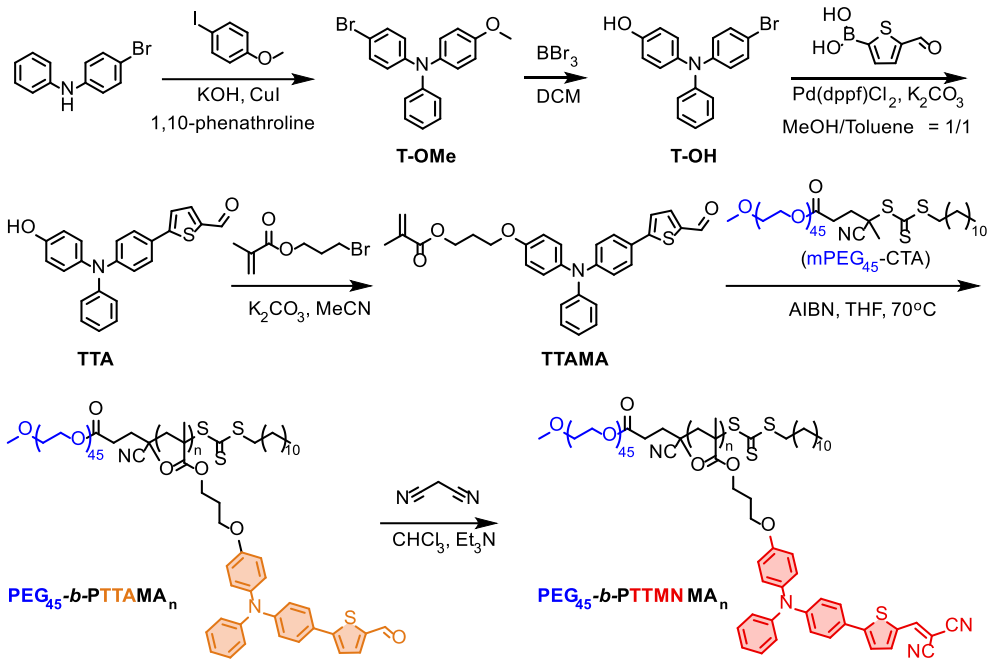

Scheme 1. Synthetic route to monomer TTAMA and the diblock copolymers PEG$_{45}$-*b*-PTTMNMA$_n$.

also hamper the likelihood of photoinduced electron transfer in the excited state necessary for photoredox catalysis.[16] To circumvent the ACQ effect, an organic dye with aggregation-induced emission (AIE) characteristics was used in this study. It is a triphenylamine-thiophene-based AIE dye (noted as TTMN) as shown in Figure 1.[26-27] The triphenylamine (TPA) moiety, a propeller-shaped nonplanar structure, can freely rotate in the solution state to result in nonradiative relaxation of excited states of the dye. However, restriction of intramolecular motions (RIMs) in aggregates blocks the nonradiative relaxation to produce enhanced emission and make the dye AIE- active.[28-29] Its typical electron-donating and -accepting (D–A) feature facilitates intramolecular charge transfer (ICT) and thus allows longer wavelength absorption (visible light) and emission (red/NIR light).[27, 30-31] The D-A effect also induces the decrease of the energy gap between the singlet excited state (S_1) and triplet excited state (T_1), and favors the intersystem crossing (ISC) process to T_1.[32-33,] Accordingly, the triplet excited state with lifetime on the order of microseconds to milliseconds should be the most relevant excited state in photoredox reactions.[16] As far as we are aware, AIE dyes with predominant triplet excited state have never been used as visible-light-mediated photoredox catalysts.

A series of amphiphilic block copolymers (PEG$_{45}$-*b*-PTTMNMA$_n$) with polyethylene glycol (PEG, degree of polymerization DP = 45) as the hydrophilic block and polymethacrylate bearing side group TTMN (PTTMNMA$_n$) as the hydrophobic block have been prepared. Polymer micelles and vesicles obtained by simple self-assembly in water have been successfully used as the visible-light-mediated photocatalyst in a photobiocatalytic system in combination with the native enzyme of glucose 1-dehydrogenase. These polymer micelles/vesicles nanophotoreactors can effectively regenerate the enzymatic cofactor NAD$^+$ under the aerobic aqueous condition without affecting the native enzyme activity. After ten consecutive regeneration cycles, the glucose 1-dehydrogenase still works as the active enzyme. This work represents a proof of concept for the use of polymer micelles/vesicles as efficient photoredox catalysts in aerobic photobiocatalysis. Other AIE dyes combined with other enzyme/cofactor pairs, especially those that make reduction of substrates, can be developed in the future to establish industrially relevant photobiocatalytic systems.

RESULTS AND DISCUSSION

Syntheses of monomers and polymers

To synthesize amphiphilic polymer PEG-*b*-PTTMNMA, two triphenylamine-thiophene (TT) based monomers, namely TTAMA and TTMNMA, were prepared by adaption of procedures reported in the literature (see Scheme 1, Scheme S1, and the supplementary information for details).[34-35] TTAMA is an aldehyde-based monomer with yellow emission, which can further react with malononitrile to afford the TTMNMA with red emission (Figure S1). All the compounds were carefully purified and characterized by ^{1}H NMR and ^{13}C NMR (see Figure S2-S6). The monomer TTMNMA was first used to directly synthesize the amphiphilic polymer PEG-*b*-PTTMNMA by reversible addition-fragmentation chain transfer (RAFT) polymerization with mPEG$_{45}$-CTA (M_n = 2400 Da) as macro-chain transfer agent and 2,2'-azobis(isobutyronitrile) (AIBN) as the initiator (Scheme S2). mPEG$_{45}$-CTA was synthesized as described in our previous work.[36] However, nearly no monomer conversion was detected by NMR spectra after 16h of reaction (Figure S7). To circumvent this problem, the monomer TTAMA was then used as the monomer to synthesize firstly PEG-*b*-PTTAMA by RAFT polymerization. PEG-*b*-PTTAMA thus successfully obtained was transformed to the target amphiphilic polymers PEG-*b*-PTTMNMA through a post-polymerization modification (a Knoevenagel condensation with malononitrile as shown in Scheme 1). All the copol-

ymers were characterized by ^{1}H NMR and size-exclusion chromatography (SEC) (see Figure S8-S12). Taking polymer PEG_{45}-*b*-$PTTMNMA_{14}$ as an example (Figure S8-S11), the SEC profile of its precursor PEG_{45}-b-$PTTAMA_{14}$ is unimodal with narrow molar mass distribution (dispersity Đ =1.15). The ^{1}H NMR spectra show the disappearance of the peak assigned to the aldehyde group of precursor PEG_{45}-*b*-$PTTAMA_{14}$, suggesting the quantitative transformation of aldehyde groups to dicyanovinyl groups after the post-modification. By adjusting feed ratios of monomer TTAMA and PEG_{45}-CTA, three amphiphilic diblock copolymers PEG_{45}-*b*-$PTTMNMA_n$ (n = 8, 14, 21) with PEG block weight ratios f_{PEG} (wt%) (PEG molar mass over the whole molar mass of the copolymer) of 28.8%, 19.6% and 14.4%, respectively, were finally prepared (see Table 1). They all display relatively narrow molar mass distributions (Đ = M_w/M_n = 1.17~1.37) as shown in the SEC curve (Figure S12).

Table 1. molar mass and molar mass distributions of copolymers PEG_{45}-*b*-$PTTMNMA_n$

Polymers	DP of TTMNMA block (n) [a]	M_n (Da) [a]	$Đ$ [b]	f_{PEG} (wt%) [a]
PEG_{45}-*b*-$PTTMNMA_{21}$	21	13900	1.37	14.4
PEG_{45}-*b*-$PTTMNMA_{14}$	14	10200	1.18	19.6
PEG_{45}-*b*-$PTTMNMA_8$	8	6900	1.17	28.8

[a] Degree of polymerization (DP) of the hydrophobic block PTTMNMA, number-average molar mass (M_n) and hydrophilic weight ratio (f_{PEG}) of the copolymer were determined by ^{1}H NMR spectroscopy.

[b] Dispersity (Đ) = M_w/M_n; M_w and M_n here were measured by SEC using DMF as eluent and monodispersed polystyrenes as calibration standards.

Preparation of polymer micelles and vesicles by self-assembly in water

The nanoprecipitation method was used to prepare the self-assemblies of diblock copolymers PEG_{45}-*b*-$PTTMNMA_n$ in water. Typically, the diblock copolymer was dissolved in 1 mL of organic cosolvent(s) at a concentration of 0.25 wt %. 5 mL of deionized water was injected *via* a syringe pump at an additional speed of 0.2 mL/h with slightly shaking. Finally, the dispersions of self-assemblies were dialyzed against water to remove the organic solvent. The self-assemblies were then characterized by cryogenic electron microscopy (cryo-EM), scanning electron microscope (SEM) and dynamic light scattering (DLS).

Effect of hydrophilic weight ratio (f_{PEG}) on the morphology of self-assemblies

Dioxane was chosen as the cosolvent to study the effect of hydrophilic ratio (f_{PEG}) on the morphology of self-assemblies of the diblock copolymers PEG_{45}-*b*-$PTTMNMA_n$ (Figure 2). The ratio f_{PEG} was changed as a function of the DP of hydrophobic block (n). As observed by cryo-EM (Figure 2A), PEG_{45}-*b*-$PTTMNMA_8$ (f_{PEG} = 28.8%) self-assembled into spherical micelles. The diameter of their hydrophobic core (*d*) was measured to be 11.6 ± 1.2 nm from the FWHM (Full width at half maximum) of the electronic density profile along the diameter through statistical analysis of 30 micelles in collected cryo-EM images. The average hydrodynamic diameter was 31 nm, as measured by DLS (Figure S13A). Further increasing the DP to n = 14 and decreasing hydrophilic ratio to 19.6% (PEG_{45}-*b*-$PTTMNMA_{14}$), micelles were still the major morphology despite the presence of a few polymer vesicles (polymersomes) (Figure 2B). The hydrophobic core diameter of micelles and the membrane thickness (hydrophobic part, *e*) of polymer vesicles were measured as *d* = 15.5± 1.3 and *e* = 7.7 ± 1.4 nm, respectively. In contrast, PEG_{45}-*b*-$PTTMNMA_{21}$ (n = 21, f_{PEG} = 14.4%) self-assembled into vesicles, as revealed by cryo-EM (Figure 2C) and further confirmed by SEM whose images show broken capsules (Figure S14). Their membrane thickness was measured as *e* = 12.5 ± 0.9 nm in cryo-EM images, and their hydrodynamic diameter (D_h) was 220 nm according to analysis by DLS (Figure S13C). The tendency of the morphological transformation from micelles to vesicles with the gradual decrease of hydrophilic ratio f_{PEG} (from 28.8% to 14.4%), is in agreement with the empirical molecular packing model from conic shape to truncated cone with the increase of the volume of hydrophobic part (see also Figure 3B below).[37]

Effect of organic co-solvent on the morphology of self-assemblies

The effect of cosolvent on the self-assembly of PEG_{45}-*b*-$PTTMNMA_8$ (f_{PEG} = 28.8%) and PEG_{45}-*b*-$PTTMNMA_{14}$ (f_{PEG} = 19.6%) was also studied by using dioxane and DMF mixtures of different volume ratios as organic solvent (Figure 2D-2F and Figure S16-S18). Recall that the PEG_{45}-*b*-$PTTMNMA_8$ (f_{PEG} = 28.8%) formed micelles in the dioxane/water system (Figure 2A). With DMF/dioxane as cosolvent at DMF fraction below 50%, PEG_{45}-*b*-$PTTMNMA_8$ still prefers to form micelles, as indicated by the SEM image in Figure S16A. The cryo-EM image in Figure 2E shows clearly the micellar structure formed by the copolymer with DMF/dioxane = 50/50. At the DMF contents of 60% and 70% (see Figure S16-S17 and Figure 2E), the vesicular structures could be found together with micelles. Further increasing the DMF fraction to 80%, only vesicles were obtained according to the collected cryo-EM images (Figure 2F). When the DMF fraction increased to 90%, the vesicles tend to coalesce to generate large compound vesicles (LCVs) as revealed by SEM and cryo-EM images (Figure S16E and S17B). The average hydrodynamic diameters of micelles and vesicles were measured by DLS (see Figure S18), their values (D_h) together with the micellar core diameters (*d*) and the membrane thicknesses (*e*) are summarized in Table S2.

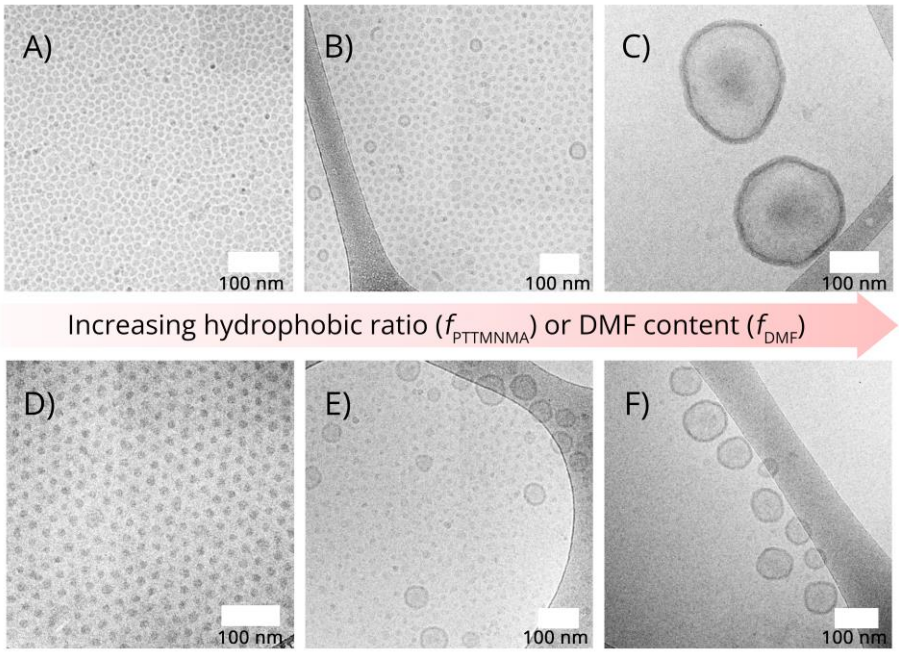

Figure 2. **Self-assembly morphologies.** Cryo-EM images (A-C) of the assemblies formed by PEG_{45}-*b*-$PTTMNMA_n$ by nanoprecipitation in dioxane/water system. (A) PEG_{45}-*b*-$PTTMNMA_8$ (f_{PEG}= 28.8%). (B) PEG_{45}-*b*-$PTTMNMA_{14}$ (f_{PEG}= 19.6%). (C) PEG_{45}-*b*-$PTTMNMA_{21}$ (f_{PEG}= 14.4%). Cryo-EM images (D-F) of the assemblies formed by PEG_{45}-*b*-$PTTMNMA_8$ in DMF/dioxane/water system with varied DMF/dioxane ratio: DMF/dioxane = 50/50 (D), 70/30 (E), 80/20 (F).

A similar tendency occurred for the self-assembly of PEG_{45}-*b*-$PTTMNMA_{14}$ (f_{PEG} = 19.6%) in the DMF/dioxane/water system. In the dioxane/water system, the PEG_{45}-*b*-$PTTMNMA_{14}$ formed micelles with the coexistence of a few small polymersomes (Figure 2B). Polymersomes became the dominant morphologies when the DMF fraction was from 25% to 55% (see cryo-EM and SEM images in Figure S19). An increasing hydrodynamic diameter (D_h) was measured by DLS: 88 nm, 79 nm and 115 nm for the DMF fraction of 25%, 40% and 55%, respectively (Figure S20). When the fraction of DMF reached 60%, LCVs were observed as shown in the cryo-EM (Figure S19I) and SEM (Figure S19J) images. All the data were summarized in Table S3.

The above results suggest that both the hydrophilic block ratio f_{PEG} and the co-solvent composition have a significant influence on the morphologies of self-assemblies, which occurs through the change of the molecular shape of block copolymers in different conditions as summarized in Figure 3. In the dioxane/water system, the polymer PEG_{45}-*b*-$PTTMNMA_8$ with f_{PEG} = 28.8% has a micelle-forming conical shape, while PEG_{45}-*b*-$PTTMNMA_{21}$ with f_{PEG} = 14.4% has vesicle-forming shape of the truncated cone. With the same ratio f_{PEG}, the dimensions of both hydrophilic and hydrophobic domains during the self-assembly process were affected by their solubility in the organic co-solvent. The Flory-Huggins interaction between polymer and solvents ($\chi_{p\text{-}s}$) can be used to evaluate their solubility. The value of $\chi_{p\text{-}s}$ < 0.5 indicates the polymer dissolves well in the solvent, and a higher value of $\chi_{p\text{-}s}$ implies relatively poor miscibility between the polymer and solvent (see SI and Table S4 for their calculation). With the increase of DMF content in DMF/dioxane mixtures from 0% to 90%, the Flory-Huggins interaction between PEG and solvent mixture ($\chi_{PEG\text{-}S}$) gradually increases from 0.34 to 0.84. It means that the hydrophilic PEG block becomes less and less swollen with the increase of DMF content. In contrast, the $\chi_{PTTMNMA\text{-}S}$ value between hydrophobic block PTTMNMA and solvent mixture stays between 0.34 – 0.43 for all solvent mixtures (except $\chi_{PTTMNMA\text{-}S}$ = 0.52 for 90% DMF) that indicates a good solubility of PTTMNMA in solvent mixtures. Consequently, the interfacial curvature towards the hydrophobic

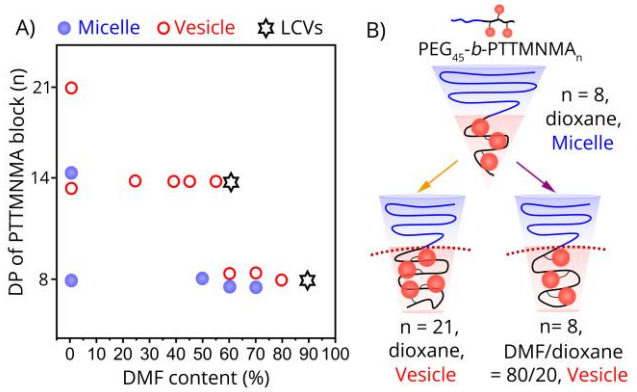

Figure 3. A) Morphological phase diagram of the self-assemblies of PEG_{45}-*b*-$PTTMNMA_n$. B) Schematic representation of the molecular shapes of PEG_{45}-*b*-$PTTMNMA_n$ with n = 8 and 21 in dioxane/water, and of PEG_{45}-*b*-$PTTMNMA_8$ in DMF/dioxane/water system with DMF/dioxane =0/100 and 80/20, resulting in micelle and vesicle, respectively.

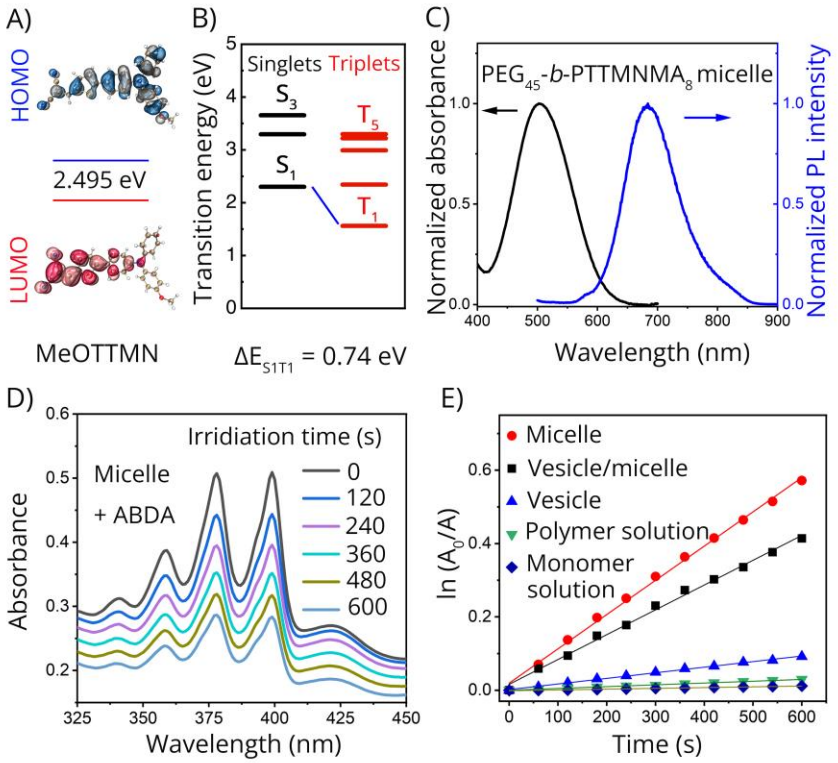

Figure 4. A) HOMO-LUMO distribution of side unit MeOTTMN of polymers PEG_{45}-*b*-$PTTMNMA_n$. B) Singlet and triplet energy levels and ΔE_{S1T1} values of side unit model MeOTTMN. C) Normalized UV-vis absorption and photoluminescence spectra of micelles formed by PEG_{45}-*b*-$PTTMNMA_8$, Excitation: 500 nm. E) The UV-visible absorption spectra of ABDA (50 μM) in the presence of PEG_{45}-*b*-$PTTMNMA_8$ micelles. D) The $\ln(A_0/A)$ as a function of irradiation time (t) for monomer TTMNMA and PEG_{45}-*b*-$PTTMNMA_{14}$ in DMF solution, and PEG_{45}-*b*-$PTTMNMA_n$ self-assemblies in water dispersion formed in dioxane/water system. A_0 and A are the absorbances of ABDA at 378 nm before (t = 0) and after irradiation (t), respectively. The slope of the fit by linear function gives the $^1O_2$ production rate (K) (s^{-1}).

core decreases with the DMF content increasing (Figure 3B). A corresponding morphological change from micelles, to vesicles, to large compound vesicles (LCVs) were observed. The increasing tendency of hydrodynamic diameters of vesicles with the increase of DMF fraction observed in PEG_{45}-*b*-$PTTMNMA_{14}$ also reflects this reduction of the interfacial curvature towards the hydrophobic core.

In summary, pure polymer micelles and vesicles could be prepared using the nanoprecipitation method either by varying the length (n) of the hydrophobic part in the block copolymer or by varying DMF content in the co-solvent mixture of DMF/dioxane. Meanwhile, the hydrodynamic diameters of polymer vesicles could also be adjusted in the window from 50 nm to 220 nm, an interesting range for their possible application in nanomedicine.

Photophysical properties of polymer micelles and vesicles

The TTMN side group possesses a typical donor-acceptor (D-A) structure with a triphenylamine (TPA) fragment serving as electron donor, a thiophene group as electron donor and π-bridge, and two cyano units as electron acceptor. This is confirmed by density functional theory (DFT) calculation of the highest occupied molecular orbital (HOMO) and the lowest unoccupied molecular orbital (LUMO) of MeOTTM, the small molecular model of luminogenic side group of PEG_{45}-*b*-$PTTMNMA_n$ (Figure 4A, MeOTTMN structure is shown in Scheme S3). The electron clouds of HOMO of MeOTTMN were rather delocalized at the TPA moiety, while those of LUMO were primarily contributed by the orbitals of dicyanovinyl and thiophene groups, indicating the separation of HOMO-LUMO and typical D-A features. The small HOMO-LUMO energy gap of 2.495 eV implies its visible light absorption and red/NIR emission properties (Figure 4C and Figure S21-S22). On the other hand, the TPA moiety is a twisted nonplanar structure, where three benzene groups can freely rotate in the solution state, thus resulting in weak emission in the solution because of nonradiative relaxation. Such a kind of relaxation could be validly blocked in the aggregated state by suppressing the intramolecular rotation. Meanwhile, the propeller shape of TPA can act as a steric impediment to prevent perfect anti-parallel stacking of dipolar chromophores upon aggregation. As such, the activation of radiative channels occurs in aggregates, leading to AIE features with red/NIR emission, which is shown in Figure S22-S24 for the monomer TTMNMA aggregates formed by adding water into its DMF solution.

The polymer micelles and vesicles are well-structured aggregates exhibiting similar photophysical behavior as TTMNMA monomer aggregates. Figure 4C and Figure S25 show the ab-

sorption and emission spectra of PEG_{45}-*b*-$PTTMNMA_n$ micelles and vesicles, with an absorption peak at around 500 nm and a maximal emission at around 680 nm. Interestingly, the maximum absorption peak of the PEG_{45}-*b*-$PTTMNMA_{21}$ vesicles red-shifted to 518 nm (Figure S25). Similar red shift in absorbance was observed for polymersomes formed by either PEG_{45}-*b*-$PTTMNMA_8$ or PEG_{45}-*b*-$PTTMNMA_{14}$ in DMF/dioxane/water system (Figure S26-27). This is probably because of the different packing models of luminogenic units within the membrane of polymersomes from those in the core of micelles. Luminescence quantum yields (Φ) of all assemblies were measured as around 0.9%, by using 4-(dicyanomethylene)-2-methyl-6-(4-dimethylaminostyryl)-4H-pyran as the standard (Φ = 43%) (Table S5).

More interestingly, such a D-A structure of TTMN unit also allows the decrease of the energy gap between the lowest excited singlet (S_1) and the lowest excited triplet (T_1). The singlet-triplet energy gap (ΔE_{S1T1}) was calculated to be around 0.74 eV, suggesting an efficient intersystem crossing (ISC) process (Figure 4B). Moreover, the suppressed molecular rotation of AIEgens in the aggregation state is beneficial for the ISC process.[33] The lifetime of the triplet excited state is normally longer than that of the singlet excited state. Then, the favored triplet excited state of the dye can be involved either in photosensitization or in photoredox catalysis. In the first case, the triplet excited state engages in energy transfer processes, particularly the "sensitization" of molecular oxygen (O_2) to produce singlet oxygen ($^1O_2$), or in electron transfer processes to produce superoxide anion radicals which can further generate hydrogen peroxide and hydroxyl radicals. All these active species are called reactive oxygen species (ROS) that can be used for photodynamic therapy (PDT) to kill cancer cells or to inactivate bacteria,[38] and the dye is normally called a photosensitizer. In the second case where the dye is called a photoredox catalyst, the triplet excited state participates in a redox reaction through electron transfer and a subsequent turnover step to return to the ground state.[16] Some organic chromophores, like rose Bengal, can be used as both photosensitizers and photoredox catalysts. The goal of this work was to investigate the possibility of using PEG_{45}-*b*-$PTTMNMA_n$ polymer nanoparticles as photoredox catalysts in a photobiocatalysis to regenerate the co-factor NAD^+ necessary for the biocatalytic activity of a related enzyme (see the next section). Beforehand, the ROS generation by these polymer nanoparticles was first evaluated, because ROS are harmful to the enzyme.

Previous works showed that singlet oxygen ($^1O_2$) was the principal ROS produced by the dye based on TTMN structure.[34] Therefore, the $^1O_2$ generation was evaluated using an indirect way with 9,10-anthracenediyl-bis(methylene)dimalonic acid (ABDA) as the indicator and rose Bengal as the standard reference (the $^1O_2$ quantum yield for rose Bengal in water is 75%). The sample solution or dispersion in the presence of ABDA was illuminated by a LED white light (see Figure S28 for LED spectrum), the light intensity on the sample being 30 $mW \cdot cm^{-2}$. The ABDA reacted with the produced $^1O_2$ to yield corresponding anthracene endoperoxide (Figure S29), which resulted in the decrease of UV-visible absorption of the indicator (Figure 4D). The $^1O_2$ production rate, equivalent to the ABDA transformation rate, could be evaluated and the $^1O_2$ quantum yields was calculated (see Method in SI and Figure S30). For monomer TTMNMN and copolymer PEG_{45}-*b*-$PTTMNMA_{14}$ in DMF solution, slow transformation rates of ABDA were observed during irradiation (Figure 4E), and their $^1O_2$ quantum yields were measured to be 0.7% and 1.9%, respectively. In contrast, PEG_{45}-*b*-$PTTMNMA_8$ micelles, PEG_{45}-*b*-$PTTMNMA_{14}$ micelles/vesicles and PEG_{45}-*b*-$PTTMNMA_{21}$ vesicles formed in dioxane/water system exhibited higher $^1O_2$ generation efficiency as they induced faster transformation of ABDA (Figure 4E), and their $^1O_2$ quantum yields were 40.6%, 28.8% and 7.2%, respectively. The relatively low value of $^1O_2$ quantum yield measured for pure polymersomes was probably due to the inefficient reaction between generated $^1O_2$ and the indicator [39], as well as the dense packing of the AIEgens in the vesicles membrane [40]. In fact, $^1O_2$ produced by the inner leaflet of the membrane might be trapped by the interior environment instead of the indicator ABDA, since ABDA added in the dispersion was essentially located outside the vesicles (see Figure S32 in SI). On the other hand, the AIEgens in vesicles packed denser than that in micelles, as indicated by the fact that the membrane thickness is smaller than the micellar diameter for the same polymer PEG_{45}-*b*-$PTTMNMA_8$ (Table S2). Dense packing of the AIEgens could induce worse oxygen diffusion inside the hydrophobic domain, then lower $^1O_2$ quantum yield. Similar results were obtained for micelles and vesicles formed in DMF/dioxane/water system (Figure S33). $^1O_2$ quantum yield measured for PEG_{45}-*b*-$PTTMNMA_8$ micelles (with DMF/dioxane =50/50) was 35.2%, while the value measured for PEG_{45}-*b*-$PTTMNMA_8$ vesicles (with DMF/dioxane = 80/20) was 21.6% (Table S6).

It is worth noting that in the photobiocatalytic system (Figure 1B) the co-factor NADH will enter in competition with the molecular oxygen as the substances that react with the triplet excited state of the dye. Therefore, the $^1O_2$ quantum yields in the photobiocatalytic system will surely be lower than the above-measured values that can be considered as the upper limits.

Polymer micelles and vesicles as photocatalysts for NAD^+ regeneration in a photobiocatalytic system

The polymer micelles and vesicles studied as photocatalysts to regenerate NAD^+ necessary for a continuous oxidation of glucose by the glucose 1-dehydrogenase were made from PEG_{45}-*b*-$PTTMNMA_8$ with 50/50 and 80/20 DMF/dioxane mixtures as organic cosolvents, respectively (see Figure 2D and 2F). Their ability as photocatalysts to regenerate NAD^+ from NADH upon visible light illumination was first examined by ^1H NMR and UV-*vis* absorption spectra. Taking the polymer vesicle as an example, the ^1H NMR spectra of NADH added in the water dispersion of

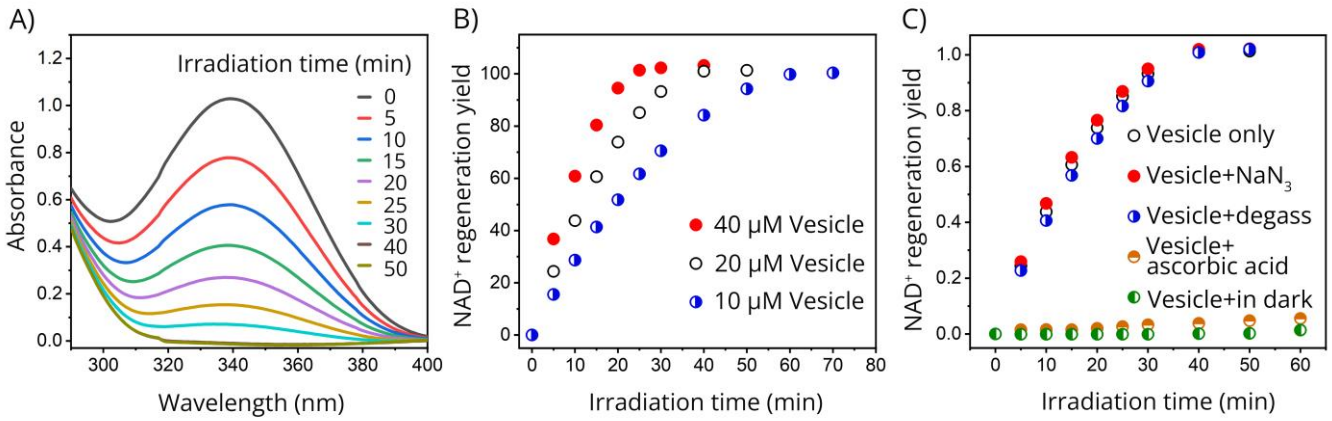

Figure 5. NAD^+ regeneration catalyzed by polymer vesicles. A) Absorbance spectra of NADH as a function of irradiation time. The reaction was performed in the dispersion of vesicles (containing 20 μM TTMN units) in PBS buffer under ambient and aerobic conditions using LED white light (30 mW/cm^2). B) NAD^+ regeneration yield at different photocatalyst concentrations of polymer vesicles (TTMN unit molar concentration, simply noted as 10, 20, 40 μM vesicles). C) NAD^+ regeneration yield catalyzed by vesicles (20 μM) under different conditions

polymer vesicles (Figure S34) show that the characteristic chemical shifts at δ = 8.43 and 8.17 ppm assigned to the adenine protons of NADH become smaller and smaller under irradiation of LED white light (30 $mW \cdot cm^2$, 400-700 nm, Figure S28). The formation of NAD^+ under irradiation was confirmed by the appearance of signals at δ = 8.77, 9.10 and 9.28 ppm corresponding to the nicotinamide group in NAD^+. This NAD^+ regeneration from NADH can also be monitored by the change of characteristic absorption peak of NADH at 340 nm (Figure S35). As shown in Figure 5A, a gradual decrease of absorption at 340 nm was observed during irradiation of polymer vesicles dispersion (containing 20 μM TTMN units) in PBS buffer under ambient and aerobic conditions. The conversion of NADH to NAD^+ as a function of illumination time (Figure 5B) could be calculated according to the NADH standard curve (Figure S36). The higher the concentration of polymer vesicle photocatalyst, the higher the NAD^+ regeneration speed is (Figure 5B, Figure S37 and Table S7). For example, 250 μM of NADH was completely oxidized in 1h by vesicles containing 10μM TTMN units, but only in 30 min by vesicles containing 40μM TTMN units. For simplicity, in the following texts, these concentrations will be written as 10μM or 40 μM vesicles (or micelles), which means the molar concentration of photocatalytic sites in vesicles (or micelles). The polymer micelles also exhibited photocatalytic activity to oxidize the NADH to NAD^+ as shown by ^1H NMR (Figure S38) and UV-*vis* absorption spectra (Figure S39). Moreover, the rates of NAD^+ regeneration were higher when catalyzed by polymer micelles than by vesicles. For example, at the concentration of 20 μM polymer nanoparticles, full conversion of NADH to NAD^+ was achieved in 30 min by micelles, but in 40 min by vesicles. The average NAD^+ generation rates catalyzed by micelles and vesicles were calculated as 665.6 and 551.8 μmol/h, respectively (Table S7). The probable reason is attributed to the incomplete contact between NADH and photocatalyst sites. The NADH was mainly located outside the vesicles and only a few NADH might enter the interior compartment of vesicles across the hydrophobic core of the membrane. Therefore, the catalytic site in the inner leaflet of the membrane could not efficiently oxidize NADH to NAD^+. As a result, lower NAD^+ regeneration rates by polymer vesicles were observed. All the results also suggest that the diffusion of NADH and NAD^+ from aqueous environment to photocatalytic sites across the hydrophilic PEG is free. A whole vesicle (or micelle) constitutes then a nanophotoreactor.

To elucidate the mechanism of the photocatalyzed NAD^+ regeneration, a series of control experiments were performed (Figure 5C and Figure S40-S41). Taking the polymer vesicle as an example, by adding 5mM of NaN_3 ($^1O_2$ quencher) to the solution, the rate of NADH oxidation was maintained (Figure S40A). Therefore, the $^1O_2$ didn't contribute to the NAD^+ regeneration. Moreover, the molecular oxygen O_2 was not essential for the NADH oxidation, because NADH oxidation still took place when the reaction system was degassed to remove the oxygen by bubbling argon (Figure S40B). In contrast, the addition of ascorbic acid (a scavenger of photogenerated hole)[19] significantly slowed down the NADH photooxidation rate (Figure S40C). Finally, light illumination was blocked to test the possible reaction in the dark. No NAD^+ was generated from NADH in the dark (Figure S40D). In conclusion, a reaction mechanism *via* electron transfer process between excited triplet state and NADH is plausible, as also proposed in the literature (Figure S42).[16, 41-42]

Figure 6A illustrates the photobiocatalytic system with the combination of polymer vesicles with glucose 1-dehydrogenase for continuous oxidation of β-D-glucose. In the biocatalytic reactions with NAD^+ as the cofactor and β-D-glucose as the substrate, β-D-glucose was oxidized to gluconolactone, while NAD^+ was reduced to NADH. Following these biocatalytic reactions, NAD^+ could be regenerated from NADH by polymer micelle/vesicle photocatalyst to sustain the catalytic cycle.

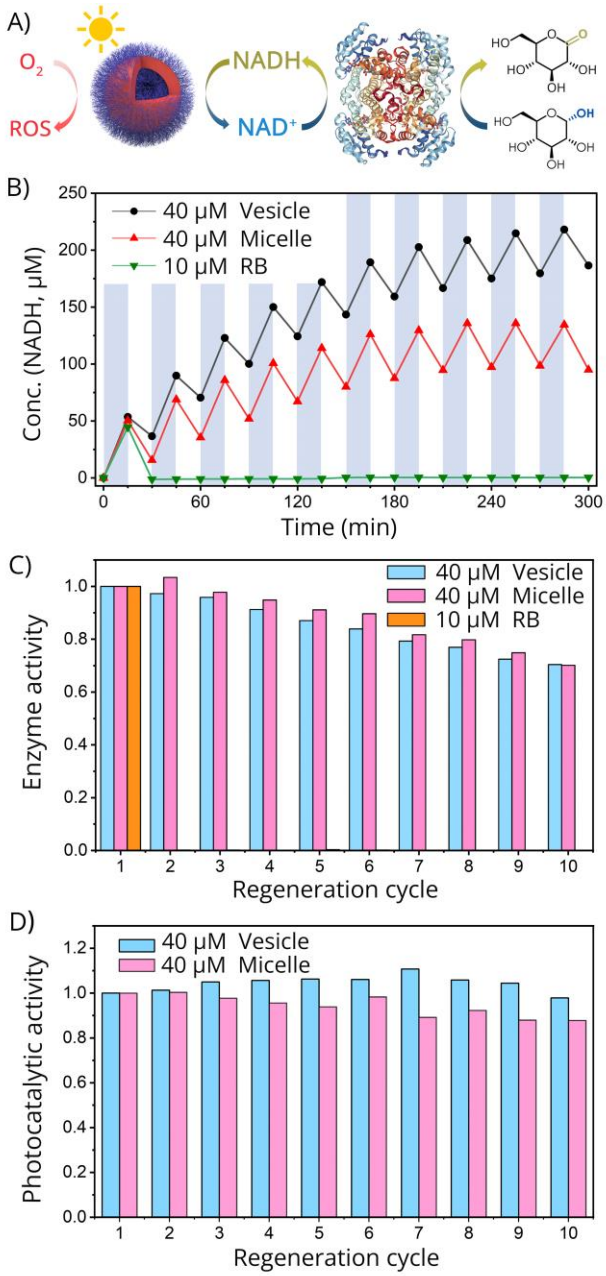

Figure 6. NAD^+ regeneration catalyzed by polymer vesicles or micelles. A) Illustration of the combination of polymer vesicle photocatalyst with glucose 1-dehydrogenase. B) The combination of glucose 1-dehydrogenase and polymer vesicle, micelles and rose Bengal photocatalysts for the generation of NADH and NAD^+ alternately by controlling the LED light "off/on". The blue shadows indicate LED off (in the dark) and no shadow ranges correspond to LED on (in the light). C) Enzymatic activity of glucose 1-dehydrogenase in the presence of vesicle, micelle and rose Bengal after each biocatalytic and photocatalytic cycle. D) Photocatalytic activity of polymer vesicles and micelles after each biocatalytic and photocatalytic cycle.

To avoid the problem of photogenerated ROS, we have first tested the biocatalytic system in an anaerobic condition by bubbling the solution with argon. Unfortunately, the biocatalytic reactions didn't occur in the absence of oxygen (see Figure S43). So, the normal aerobic condition was used. Initially, NAD^+, glucose, glucose 1-dehydrogenase and polymer micelle/vesicle were added into PBS buffer in the dark (see method part and Figure S44 in SI). For the first biocatalytic cycle, selective oxidation of glucose to gluconolactone occurred in the dark together with the reduction of NAD^+ to NADH, the NADH concentration being monitored after 15 min of reaction (see the points at t = 15 min in Figure 6B). Afterwards, the mixtures were irradiated with the white LED light (30 mW/cm^2) for 15min. A decrease in the NADH concentration was observed because of the photocatalyzed regeneration of NAD^+ from NADH (see the points at t = 30 min in Figure 6B). This is the first complete biocatalytic and photocatalytic cycle. The variation of NADH concentration (up and down) also suggested that the photocatalytic regeneration of NAD^+ from NADH was faster than its reverse reaction involved the enzymatic reaction, because photocatalyzed NADH to NAD^+ reaction occurred only upon light illumination, while enzyme catalyzed NAD^+ to NADH reaction occurred both in the dark and in the light. For comparison, the data using micelle, vesicle and rose Bengal (reference) as photocatalysts are presented in the same graph (Figure 6B). In the system with rose Bengal, it is interesting to observe that upon the first cycle of light illumination the concentration of NADH was completely returned to zero. Very likely, the enzymatic reaction was already depressed in the first light cycle. Then the LED was switched off to start the second biocatalytic and photocatalytic cycle, and so on. Each cycle was composed of 15 min in the dark and 15 min in the light before the monitoring of NADH concentration. With rose Bengal, no NADH was produced in the second biocatalytic cycle (see green triangle at t = 45 min), indicating the enzyme was deactivated. This result also confirmed the above observation for the first light cycle. The photogenerated ROS by rose Bengal in the first photocatalytic cycle had damaged the enzyme. Note that rose Bengal is soluble in PBS aqueous solution, and the produced ROS can freely diffuse to get in contact with the enzyme. In contrast, in the systems with polymer micelles and vesicles, the NADH was produced in successive biocatalytic cycles following photocatalytic cycles (see red and black points and curves in Figure 6B). Therefore, the enzyme remained active, despite the presence of ROS photogenerated by micelle and vesicle. As a matter of fact, ROS have a very limited lifetime and diffusion distance. For example, the lifetime of $^1O_2$ in aqueous solution is about 3.1 μs.[43] Within this time span, its diffusion is possible only within a radius estimated in the order of 10 nm.[44-45] Given that micelles and vesicles have a very dense PEG layer at the surface (PEG is attached to each hydrophobic block), the PEG may adopt squeezed conformation at micelle and vesicle surfaces with thickness H: $2R_g < H < L$, where R_g is the radius of gyration of PEG in water and L the fully extended length of PEG.[46] As the PEG_{45} (M_n=2000 Da) has a R_g of 4.3 nm,[47] and a L estimated as 12.5 nm,[48] the PEG thickness H is 8.6 nm < H < 12.5 nm, thus in the same order of the limit of ROS diffusion distance (Figure 1B). Considering the larger size of enzyme, it is unlikely for enzyme to diffuse into the dense hydrophilic PEG layer. Therefore, the hydrophilic layer plays effectively the role of a barrier to prevent the contact between ROS species and enzyme and to preserve the enzymatic activity. As shown in Figure 6B, the enzyme still works well after 10 photocatalytic and biocatalytic cycles in

the photobiocatalytic system. Over 70% of enzyme activity is preserved after 10 cycles as shown in Figure 6C, and only around 3% of enzyme activity loss occurs per cycle, which is probably caused by minor amount of ROS escaped from the PEG layer.

The photocatalytic activities of polymer micelles and vesicles are 85% and 98%, respectively, after 10 cycles with 150 min LED illumination in total (Figure 6D). This suggests that polymer micelles and vesicles have very good photostability and catalytic performance. Figure S45 shows that the polymer micelles exhibit good chemical structure stability after 1 h of continuous irradiation. These photocatalysts are also very stable in an aqueous solution, Figure S46 showing the vesicle size stability with 2 months of storage (at 4°C). The photobiocatalytic approach also works when we combine the polymer micelles with glycerol dehydrogenase to convert glycerol to dihydroxyacetone (Figure S47). The enzyme glycerol dehydrogenase and micelles photocatalyst still work well after 10 regenerations photocatalytic and biocatalytic cycles.

In summary, an environmentally friendly photobiocatalytic system has been developed using AIE polymer micelles and vesicles as photocatalysts. Moreover, considering that the absorption of these photocatalysts is in the range of visible light, still less damage to the biological system is ensured compared to photocatalysts activated by UV light. These photocatalyst systems may also have the potential to manipulate cofactor balance in vivo to regulate metabolic flux in a controlled way.[49-50]

CONCLUSION

Three amphiphilic polymers PEG_{45}-*b*-$PTTMNMA_n$ (n = 8, 14, 21) with hydrophilic ratios (f_{PEG}) of 28.8, 19.6 and 14.4% have been synthesized. They formed micelles, vesicle/micelle mixtures, and vesicles, respectively, using the nanoprecipitation method in water with dioxane as co-solvent. In addition, the morphology of these polymer self-assemblies and the size of polymer vesicles could also be adjusted by the composition of cosolvent mixtures. Pure polymer micelles and vesicles were prepared by the same polymer PEG_{45}-*b*-$PTTMNMA_8$ just by varying DMF/dioxane ratio in the solvent mixture of DMF and dioxane (50/50 for micelle and 80/20 for vesicle formation). The size of polymer vesicles ranging from 50 nm to 220 nm, interesting sizes for their possible application in nanomedicine, were also obtained by changing the DMF/dioxane ratio.

Thanks to the relatively low HOMO-LUMO energy gap, efficient ISC process and AIE feature of TTMN side group, the PEG_{45}-*b*-$PTTMNMA_n$ self-assemblies exhibited interesting photophysical properties, such as visible light absorption and red/NIR emission. Most importantly, their excited triplet states could play both the role of photosensitizers to produce ROS and the role of photocatalysts to catalyze redox reactions.

The polymer micelles and vesicles have been successfully used as visible-light-mediated photocatalysts for the regeneration of enzyme cofactor NAD^+ in a photobiocatalytic system in an aqueous solution at ambient and aerobic conditions. In the presence of NAD^+, glucose 1-dehydrogenase catalyzes the selctive oxidation of glucose; the process is accompanied by the reformation of NADH. After the biocatalytic cycles, the polymer colloidal photocatalysts regenerate the cofactor NAD^+ from NADH. In the core-shell structure of micelles and vesicles, the ROS photogenerated in the same time of the photocatalytic reactions are screened by the dense PEG coat on their surfaces, which preserves the activity of the native enzyme. This photobiocatalytic cycle could be repeated over at least ten consecutive cycles. The enzyme, maintained in its active state, exhibits over 70% of enzymatic activity after 10 cycles. The photocatalytic activities of polymer vesicles and micelles are 98% and 85%, respectively, after 10 cycles, ensuring highly efficient NAD^+ regeneration from NADH. In principle, these polymer colloidal photocatalysts could be used to combine with any kind of NAD^+ dependent enzyme, which may pave the way to establish industrially relevant photobiocatalytic system in the future, or to regulate metabolic flux in vivo in a controlled way. Since many synthetically useful reactions that are catalyzed by oxidoreductases require the reduced form of the cofactor (NADH) rather than the oxidized form (NAD^+),[1] the research on photobiocatalytic systems including polymer micelles and vesicles for NADH regeneration in enzymatic reduction reactions is in progress in our laboratory.

EXPERIMENTAL/METHODS

Synthesis of polymer PEG-*b*-PTTMNMA. Taking PEG_{45}-*b*-$PTTMNMA_{14}$ as an example was described as follows: The monomer TTAMA (150mg, 0.3mmol), mPEG-CTA (64.3mg, 0.027mmol) and AIBN (0.88mg, 0.005mmol) were added into a 25 mL Schlenk tube equipped with a Teflon coated stirring bar. Then 2 mL distilled THF was added. After the solution was clear, the Schlenk tube was degassed by three freeze-pump-thaw cycles. The mixture was stirred at 70 ℃ for 16h. The polymerization was terminated by freezing the mixture in liquid nitrogen. The mixture was then poured drop wisely into cold 2-propanol to obtain the crude copolymer precipitate (PEG_{45}-*b*-$PTTAMA_{14}$). The precipitate was collected by centrifugation. Then the polymer (1.0 eq) and Et_3N (two drops) were dissolved in 20 mL chloroform before the addition of malononitrile (10 eq) solution. The reaction mixture was stirred at room temperature. After 4h, the solvent was removed by vacuum. The residue was purified by precipitation in 2-propanol two times to recover the pure product as a red solid (PEG_{45}-*b*-$PTTMNMA_{14}$).

Nanoprecipitation. Around 2.3 mg of the diblock copolymer was dissolved in 1 mL of organic solvent (or organic solvent mixtures). A total volume of 5mL of deionized water was injected slowly at the rate of 200 μL/h with slight shaking. The whole process of nanoprecipitation was carried out at room temperature. The obtained turbid mixtures were then dialyzed against deionized water for 3 days to remove the organic solvent using a Spectra/Por® regenerated cellulose membrane with a molecular weight cutoff (MWCO) of 3500 Da.

The photobiocatalytic system with the combination of polymer micelle/vesicle and glucose dehydrogenase. To a 3.5 mL quartz cuvette, NAD^+ (1 mmol/L), polymer micelles or vesicles (20 or 40 μM), glucose dehydrogenase (0.1 μg/mL), 2 mL phosphate buffer (50 mmol/L, pH 7.4) were added. To start the reaction, glucose (5 mmol/L) was added to the mixture under dark condition. UV absorbance of the mixture was

recorded after keeping it in dark for 15 min. After that, a white-LED (400-700 nm, 30 mW/cm^2) was used to irradiate the sample mixtures for another 15 min. UV absorbance of the mixture was measured. This is the first biocatalytic and photocatalytic cycle. Ten cycles were conducted.

ASSOCIATED CONTENT

Supporting Information. ^{1}H NMR and ^{13}C NMR spectra of all compounds. GPC of the synthesized polymer. UV-vis and PL spectra of polymer assemblies. This material is available free of charge via the Internet at http://pubs.acs.org.

AUTHOR INFORMATION

Corresponding Author

* Dr. Min-Hui LI : min-hui.li@chimieparistech.psl.eu
* Dr. Hui CHEN: chenhui0706@outlook.com

Author Contributions

All authors have given approval to the final version of the manuscript.

ACKNOWLEDGMENT

This work is financially supported by the CNRS through the MITI interdisciplinary programs and the French National Research Agency (ANR-16-CE29-0028). The China Scholarship Council (CSC) is gratefully acknowledged by Nian Zhang for funding her respective PhD scholarships. We thank Ryan T. K. Kwok for fruitful discussions about AIEgens with Far-Red/Near-Infrared Emission. The Multimodal Imaging Centre of Institut Curie is acknowledged for providing access to cryo-EM facility in Orsay.

REFERENCES

1. Maciá-Agulló, J. A.; Corma, A.; Garcia, H., Photobiocatalysis: The Power of Combining Photocatalysis and Enzymes. *Eur. J. Chem.* **2015,** *21* (31), 10940-10959.
2. Kumar, K.; Das, D., Co2 Sequestration and Hydrogen Production Using Cyanobacteria and Green Algae. In *Natural and Artificial Photosynthesis*, John Wiley & Sons: 2013; pp 173-215.
3. Lee, S. H.; Choi, D. S.; Kuk, S. K.; Park, C. B., Photobiocatalysis: Activating Redox Enzymes by Direct or Indirect Transfer of Photoinduced Electrons. *Angew. Chem. Int. Ed.* **2018,** *57* (27), 7958-7985.
4. Kroutil, W.; Mang, H.; Edegger, K.; Faber, K., Recent Advances in the Biocatalytic Reduction of Ketones and Oxidation of Sec-Alcohols. *Curr. Opin. Chem. Biol.* **2004,** *8* (2), 120-126.
5. Wu, H.; Tian, C.; Song, X.; Liu, C.; Yang, D.; Jiang, Z., Methods for the Regeneration of Nicotinamide Coenzymes. *Green Chem.* **2013,** *15* (7), 1773-1789.
6. Monti, D.; Ottolina, G.; Carrea, G.; Riva, S., Redox Reactions Catalyzed by Isolated Enzymes. *Chem. Rev.* **2011,** *111* (7), 4111-4140.
7. Xu, F., Applications of Oxidoreductases: Recent Progress. *Ind. Biotechnol.* **2005,** *1* (1), 38-50.
8. de Miranda, A. S.; Milagre, C. D.; Hollmann, F., Alcohol Dehydrogenases as Catalysts in Organic Synthesis. *Front. Catal.* **2022**, 9.
9. Wu, S.; Snajdrova, R.; Moore, J. C.; Baldenius, K.; Bornscheuer, U. T., Biocatalysis: Enzymatic Synthesis for Industrial Applications. *Angew. Chem. Int. Ed.* **2021,** *60* (1), 88-119.
10. Rehn, G.; Pedersen, A. T.; Woodley, J. M., Application of Nad (P) H Oxidase for Cofactor Regeneration in Dehydrogenase Catalyzed Oxidations. *J. Mol. Catal. B Enzym.* **2016,** *134*, 331-339.
11. Munro, A. W.; McLean, K. J., Electron Transfer Cofactors. In *Encyclopedia of Biophysics*, Roberts, G. C. K., Ed. Springer Berlin Heidelberg: Berlin, Heidelberg, 2013; pp 601-606.
12. Zhao, H.; Van Der Donk, W. A., Regeneration of Cofactors for Use in Biocatalysis. *Curr. Opin. Biotechnol.* **2003,** *14* (6), 583-589.
13. Hollmann, F.; Hofstetter, K.; Schmid, A., Non-Enzymatic Regeneration of Nicotinamide and Flavin Cofactors for Monooxygenase Catalysis. *Trends Biotechnol.* **2006,** *24* (4), 163-171.
14. Quinto, T.; Köhler, V.; Ward, T. R., Recent Trends in Biomimetic Nadh Regeneration. *Top Catal.* **2014,** *57* (5), 321-331.
15. Prier, C. K.; Rankic, D. A.; MacMillan, D. W. C., Visible Light Photoredox Catalysis with Transition Metal Complexes: Applications in Organic Synthesis. *Chem. Rev.* **2013,** *113* (7), 5322-5363.
16. Romero, N. A.; Nicewicz, D. A., Organic Photoredox Catalysis. *Chem. Rev.* **2016,** *116* (17), 10075-10166.
17. Zhang, Y.; Zhao, Y.; Li, R.; Liu, J., Bioinspired Nadh Regeneration Based on Conjugated Photocatalytic Systems. *Solar RRL* **2021,** *5* (2), 2000339.
18. Peters, R. J.; Marguet, M.; Marais, S.; Fraaije, M. W.; van Hest, J. C.; Lecommandoux, S., Cascade Reactions in Multicompartmentalized Polymersomes. *Angew. Chem. Int. Ed.* **2014,** *53* (1), 146-50.
19. Ma, B. C.; Caire da Silva, L.; Jo, S.-M.; Wurm, F. R.; Bannwarth, M. B.; Zhang, K. A. I.; Sundmacher, K.; Landfester, K., Polymer-Based Module for Nad+ Regeneration with Visible Light. *ChemBioChem* **2019,** *20* (20), 2593-2596.
20. Jo, S.-M.; Zhang, K. A. I.; Wurm, F. R.; Landfester, K., Mimic of the Cellular Antioxidant Defense System for a Sustainable Regeneration of Nicotinamide Adenine Dinucleotide (Nad). *ACS Appl. Mater. Interfaces* **2020,** *12* (23), 25625-25632.
21. Wei, W.; Mazzotta, F.; Lieberwirth, I.; Landfester, K.; Ferguson, C. T. J.; Zhang, K. A. I., Aerobic Photobiocatalysis Enabled by Combining Core–Shell Nanophotoreactors and Native Enzymes. *J. Am. Chem. Soc.* . **2022,** *144* (16), 7320-7326.
22. Rodriguez-Jimenez, S.; Song, H.; Lam, E.; Wright, D.; Pannwitz, A.; Bonke, S. A.; Baumberg, J. J.; Bonnet, S.; Hammarstrom, L.; Reisner, E., Self-Assembled Liposomes Enhance Electron Transfer for Efficient Photocatalytic Co2 Reduction. *J. Am. Chem. Soc.* **2022,** *144* (21), 9399-9412.
23. Song, H.; Amati, A.; Pannwitz, A.; Bonnet, S.; Hammarstrom, L., Mechanistic Insights into the Charge Transfer Dynamics of Photocatalytic Water Oxidation at the Lipid Bilayer-Water Interface. *J. Am. Chem. Soc.* **2022,** *144* (42), 19353-19364.
24. Pannwitz, A.; Klein, D. M.; Rodriguez-Jimenez, S.; Casadevall, C.; Song, H.; Reisner, E.; Hammarstrom, L.; Bonnet, S., Roadmap Towards Solar Fuel Synthesis at the Water Interface of Liposome Membranes. *Chem. Soc. Rev.* **2021,** *50* (8), 4833-4855.
25. v. Bünau, G., J. B. Birks: Photophysics of Aromatic Molecules. Wiley-Interscience, London 1970. 704 Seiten. Preis: 210s. *Berichte der Bunsengesellschaft für physikalische Chemie* **1970,** *74* (12), 1294-1295.
26. Wang, D.; Su, H.; Kwok, R. T. K.; Shan, G.; Leung, A. C. S.; Lee, M. M. S.; Sung, H. H. Y.; Williams, I. D.; Lam, J. W. Y.; Tang, B. Z., Facile Synthesis of Red/Nir Aie Luminogens with Simple Structures, Bright Emissions, and High Photostabilities, and Their Applications for Specific Imaging of Lipid Droplets and Image-Guided Photodynamic Therapy. *Adv. Funct. Mater.* **2017,** *27* (46), 1704039.
27. Xu, W.; Lee, M. M. S.; Nie, J.-J.; Zhang, Z.; Kwok, R. T. K.; Lam, J. W. Y.; Xu, F.-J.; Wang, D.; Tang, B. Z., Three-Pronged Attack by Homologous Far-Red/Nir Aiegens to Achieve 1+1+1>3 Synergistic Enhanced Photodynamic Therapy. *Angew. Chem. Int. Ed.* **2020,** *59* (24), 9610-9616.
28. Mei, J.; Leung, N. L.; Kwok, R. T.; Lam, J. W.; Tang, B. Z., Aggregation-Induced Emission: Together We Shine, United We Soar! *Chem. Rev.* **2015,** *115* (21), 11718-11940.

29. Luo, J.; Xie, Z.; Lam, J. W.; Cheng, L.; Chen, H.; Qiu, C.; Kwok, H. S.; Zhan, X.; Liu, Y.; Zhu, D., Aggregation-Induced Emission of 1-Methyl-1, 2, 3, 4, 5-Pentaphenylsilole. *Chem. Comm.* **2001,** (18), 1740-1741.

30. Sissa, C.; Parthasarathy, V.; Drouin-Kucma, D.; Werts, M. H. V.; Blanchard-Desce, M.; Terenziani, F., The Effectiveness of Essential-State Models in the Description of Optical Properties of Branched Push–Pull Chromophores. *Phys. Chem. Chem. Phys.* **2010,** *12* (37), 11715-11727.

31. Xu, W.; Lee, M. M. S.; Zhang, Z.; Sung, H. H. Y.; Williams, I. D.; Kwok, R. T. K.; Lam, J. W. Y.; Wang, D.; Tang, B. Z., Facile Synthesis of Aiegens with Wide Color Tunability for Cellular Imaging and Therapy. *Chem. Sci.* **2019,** *10* (12), 3494-3501.

32. Xu, S.; Yuan, Y.; Cai, X.; Zhang, C.-J.; Hu, F.; Liang, J.; Zhang, G.; Zhang, D.; Liu, B., Tuning the Singlet-Triplet Energy Gap: A Unique Approach to Efficient Photosensitizers with Aggregation-Induced Emission (Aie) Characteristics. *Chem. Sci.* **2015,** *6* (10), 5824-5830.

33. Yang, L.; Wang, X.; Zhang, G.; Chen, X.; Zhang, G.; Jiang, J., Aggregation-Induced Intersystem Crossing: A Novel Strategy for Efficient Molecular Phosphorescence. *Nanoscale* **2016,** *8* (40), 17422-17426.

34. Wang, D.; Su, H.; Kwok, R. T. K.; Shan, G.; Leung, A. C. S.; Lee, M. M. S.; Sung, H. H. Y.; Williams, I. D.; Lam, J. W. Y.; Tang, B. Z., Facile Synthesis of Red/Nir Aie Luminogens with Simple Structures, Bright Emissions, and High Photostabilities, and Their Applications for Specific Imaging of Lipid Droplets and Image-Guided Photodynamic Therapy. *Advanced Functional Materials* **2017,** *27* (46).

35. Zhang, N.; Chen, H.; Fan, Y.; Zhou, L.; Trépout, S.; Guo, J.; Li, M.-H., Fluorescent Polymersomes with Aggregation-Induced Emission. *ACS Nano* **2018,** *12* (4), 4025-4035.

36. Chen, H.; Fan, Y.; Zhang, N.; Trépout, S.; Ptissam, B.; Brûlet, A.; Tang, B. Z.; Li, M.-H., Fluorescent Polymer Cubosomes and Hexosomes with Aggregation-Induced Emission. *Chem. Sci.* **2021,** *12* (15), 5495-5504.

37. Blanazs, A.; Armes, S. P.; Ryan, A. J., Self-Assembled Block Copolymer Aggregates: From Micelles to Vesicles and Their Biological Applications. *Macromol. Rapid Commun.* **2009,** *30* (4-5), 267-277.

38. Abrahamse, H.; Hamblin, Michael R., New Photosensitizers for Photodynamic Therapy. *Biochem. J.* **2016,** *473* (4), 347-364.

39. Zhang, Z.; Chen, H.; Wang, Y.; Zhang, N.; Trepout, S.; Tang, B. Z.; Gasser, G.; Li, M. H., Polymersomes with Red/near-Infrared Emission and Reactive Oxygen Species Generation. *Macromol. Rapid Commun.* **2022**, e2200716.

40. Cai, X.; Mao, D.; Wang, C.; Kong, D.; Cheng, X.; Liu, B., Multifunctional Liposome: A Bright Aiegen-Lipid Conjugate with Strong Photosensitization. *Angew. Chem. Int. Ed.* **2018,** *57* (50), 16396-16400.

41. Ma, B. C.; Caire da Silva, L.; Jo, S. M.; Wurm, F. R.; Bannwarth, M. B.; Zhang, K. A. I.; Sundmacher, K.; Landfester, K., Polymer-Based Module for Nad(+) Regeneration with Visible Light. *Chembiochem* **2019,** *20* (20), 2593-2596.

42. Liao, H. X.; Jia, H. Y.; Dai, J. R.; Zong, M. H.; Li, N., Bioinspired Cooperative Photobiocatalytic Regeneration of Oxidized Nicotinamide Cofactors for Catalytic Oxidations. *ChemSusChem* **2021,** *14* (7), 1687-1691.

43. Egorov, S. Y.; Kamalov, V. F.; Koroteev, N. I.; Krasnovsky, A. A.; Toleutaev, B. N.; Zinukov, S. V., Rise and Decay Kinetics of Photosensitized Singlet Oxygen Luminescence in Water. Measurements with Nanosecond Time-Correlated Single Photon Counting Technique. *Chem. Phys. Lett.* **1989,** *163* (4), 421-424.

44. Moan, J., On the Diffusion Length of Singlet Oxygen in Cells and Tissues. *J. Photochem. Photobiol. B, Biol.* **1990,** *6* (3), 343-344.

45. Sies, H.; Menck, C. F. M., Singlet Oxygen Induced DNA Damage. *Mutation Research/DNAging* **1992,** *275* (3), 367-375.

46. Tockary, T. A.; Osada, K.; Chen, Q.; Machitani, K.; Dirisala, A.; Uchida, S.; Nomoto, T.; Toh, K.; Matsumoto, Y.; Itaka, K.; Nitta, K.; Nagayama, K.; Kataoka, K., Tethered Peg Crowdedness Determining Shape and Blood Circulation Profile of Polyplex Micelle Gene Carriers. *Macromolecules* **2013,** *46* (16), 6585-6592.

47. Linegar, K. L.; Adeniran, A. E.; Kostko, A. F.; Anisimov, M. A., Hydrodynamic Radius of Polyethylene Glycol in Solution Obtained by Dynamic Light Scattering. *Colloid J.* **2010,** *72* (2), 279-281.

48. Oesterhelt, F.; Rief, M.; Gaub, H. E., Single Molecule Force Spectroscopy by Afm Indicates Helical Structure of Poly(Ethylene-Glycol) in Water. *New J. Phys.* **1999,** *1*, 6-6.

49. Tan, Z.; Zhu, C.; Fu, J.; Zhang, X.; Li, M.; Zhuang, W.; Ying, H., Regulating Cofactor Balance in Vivo with a Synthetic Flavin Analogue. *Angew. Chem. Int. Ed.* **2018,** *57* (50), 16464-16468.

50. Huang, H.; Banerjee, S.; Qiu, K.; Zhang, P.; Blacque, O.; Malcomson, T.; Paterson, M. J.; Clarkson, G. J.; Staniforth, M.; Stavros, V. G.; Gasser, G.; Chao, H.; Sadler, P. J., Targeted Photoredox Catalysis in Cancer Cells. *Nat. Chem.* **2019,** *11* (11), 1041-1048.

Table of contents